

of the main geometric and geomaterial parameters, but without considering the potential time-dependent deformations (creep effect) that occur in some types of rock masses.

Chen et al. [9], through analytical solutions in elasticity using complex variables, Fourier transformation, and the alternating Schwarz method, demonstrate that the mutual interaction between twin tunnels disappears if the spacing between the tunnels is greater than six times the tunnel radius. The lining effectively reduces the stress concentration, especially at high lateral stress coefficients.

Guo et al. [17] develop an elastic analytical solution for the stress field around twin circular tunnels with hydrostatic pressure using the complex variable and the superposition principle. They found that stress concentration in tunnel wall increased as the distance between the parallel tunnels decreased and the supporting pressure leads to the radial stress increasing and the tangential stress decreasing.

Ma et al. [18] proposed an analytical method, verified by a numerical solution using FLAC3D software for determining the plastic zones around deep circular twin tunnels without linings, restricting themselves where there is no overlap between the two plastic zones. In this case, the authors adopted the elastoplastic perfectly constitutive model for the homogeneous and isotropic rock mass, with the Mohr-Coulomb criterion. Also carried out parametric studies to understand the influence of the distance between the twin tunnels, cohesion, the angle of internal friction, and the vertical and horizontal initial stresses acting on the shape and depth of the plastic zones. These authors stated that the plastic zone around the tunnel provides a relevant theoretical basis for defining and designing the support. In that respect, an excessive plastic zone would significantly affect the stability and functionality of a tunnel. Reducing the extension of the plastic zone around tunnels is, therefore, of great importance in engineering tunnel design projects.

Using parametric three-dimensional numerical analyses, Chortis and Kavvadas [12, 13] investigated the effect of building a transverse tunnel that intersected deep twin tunnels perpendicularly, focusing the study on the axial forces and the circumferential and longitudinal bending moments acting on the primary support of the intersection regions, respectively. According to the authors, the potential interaction between deep twin tunnels lined with shotcrete must be taken into account, especially when the distance between them is less than or equal to twice their diameter.

According to Fortsakis [15], in a realistic construction context, twin tunnels are excavated and supported with a delay, so that the second tunnel is usually built after the first one has advanced enough to maintain a longitudinal separation distance between the faces. The advance of the subsequent tunnel mobilizes the redistribution of stresses and deformations in the zone between the tunnels, resulting in additional loading of the preceding tunnel.

As for transverse tunnels, these are generally built far enough behind the advanced face of the main tunnel to ensure that their excavation has virtually no effect during the construction of the junction tunnel [10]. The interaction at the intersection, between the main tunnel and the transverse tunnel, significantly modifies the stress state of the primary support and that of the surrounding rock mass in these areas, compared to that of the singular tunnel, making three-dimensional finite element analyses essential for developing a realistic and safe design for tunnel junctions [30].

During the construction of the transverse tunnel, the surrounding rock mass is subjected to a redistribution of stresses, causing an additional load on the main tunnel, precisely in the intersection zone. If these additional loads exceed the load capacity of the primary support of the main tunnel, a potentially unstable region can develop, leading to failure, especially in adverse geotechnical conditions [10].

While the simulation of tunnel convergence in single tunnels has been widely investigated and reported in published literature, few works have addressed the computational evaluation of deformation in twin tunnels. Less attention has been dedicated to assessing the mutual mechanical interaction induced by the excavation of the transverse gallery connecting the twin tunnels.

In this context, the main contributions of this paper may be summarized at both the material and tunnel analysis levels. At the material level, the constitutive state equations of the rock mass are formulated within the framework of coupled plasticity-viscoplasticity, which is relevant for clayey rocks. Such a framework allows capturing the irreversible instantaneous tunnel response (plasticity) as well as the delayed irreversible response (viscoplasticity). As regards the mechanical behavior of concrete material defining the lining, which is classically modeled through linear elastic relationships, the present analysis considers an aging viscoelastic rheological model relying upon the Bažant and Prasannan Solidification theory [3; 4]. At the structure analysis level, the simulation of deformation in the highly interacting material system components (namely, rock mass and lining), resulting from the excavation process of twin tunnels and transverse gallery, is handled using finite element simulations performed in a three-dimensional setting. From the computational viewpoint, the excavation process and lining placement are simulated by means of the activation/deactivation technique. The constitutive models formulated for the rock mass and lining constituent as well as the related numerical integration schemes are implemented into the same procedure UPF/USERMAT

customization tool [2] of ANSYS standard software. The three-dimensional finite element analysis developed in this paper is specifically devised for addressing the three-dimensional interaction induced by the construction process, twin tunnels proximity, and the presence of the transverse gallery.

2. Fundamental assumptions

The basic assumptions of the constitutive and computational modeling, as well as related limitations, are summarized as follows:

- (a) Only the configuration of deep tunnels shall be considered in the subsequent analysis, thus neglecting deformations caused by surface loads and settlements arising from the excavation process;
- (b) Although material heterogeneity and behavior anisotropy are inherent features of soils and rocks, the rock mass is modeled throughout the paper as a homogeneous and isotropic continuous medium. At the scale adopted for tunnel modeling (macroscopic scale), this assumption means in particular that the possible micro-heterogeneities, such as isotropic distributions of joints or cracks present at the finer scale, are accounted for in the homogenized behavior by means of a preliminary homogenization process (e.g., [20, 14, 7, 19, 1]). Clearly enough, the framework of continuum modeling adopted in the paper would reveal questionable when the rock mass is cut by a few macro-scale fracture joints;
- (c) The rock mass is phenomenologically modeled using an elastoplastic-viscoplastic rheological law to capture instantaneous and long-term responses. This approach disregards the aspect connected temperature gradients, water flow, and poromechanics coupling;
- (d) Despite the complexity of the stress distribution prevailing in the rock mass before the process of tunnel excavation, which is mainly affected by the geological history, the present study assumes a geostatic initial stress reflected by an isotropic state of stress.
- (e) Twin tunnels are often designed considering a time gap between excavation fronts. However, the finite element simulations assume synchronous excavation steps to ensure symmetry conditions.
- (f) The simulation excavation processes are carried out assuming a constant tunnel advancement rate (i.e., constant excavation speed), together with a constant thickness of concrete lining.
- (g) Effects of temperature and humidity that may affect the viscoelastic behavior of concrete lining are disregarded.
- (h) Perfect bonding is assumed at the interface between concrete lining and the rock mass.
- (i) The framework of infinitesimal strain analysis, together with quasi-static evolutions, is adopted in the paper. In particular, dynamic excitations and related inertial forces, such as those induced, for instance, by earthquakes or explosions, shall not be considered in the numerical analysis.

3. Constitutive Model of the Rock Material

Time-dependent phenomena associated with the delayed behavior of the constitutive material are key aspects of deformation in tunnel structures excavated in deep clayey rocks (see for instance [29, 21] or [16], to cite a few). In most computational analyses developed for tunnel engineering design, this issue is generally addressed by means of viscoplastic constitutive behavior. While such constitutive models could relevantly model the transient and long-term deformation, they seem however inadequate to capture the influence of short-term events (tunnelling and support placement phases) on the final stability of the structure. In particular, an analysis of tunnel deformation based on a viscoplastic model would suggest that the ultimate support pressure at tunnel structure equilibrium mainly depends on the closure rate at the moment when the contact between lining and rock mass is achieved (e. g., [21]), thus disregarding the irreversible effects rising in the initial construction phases. Indeed, during the primary stages of tunnel excavation, the surrounding rock mass is subjected to severe loading conditions and high strain rates, which may lead to yielding associated with high instantaneous irreversible strains near the tunnel wall, and can therefore affect the long-term equilibrium of the structure. It is thus of fundamental concern to formulate a constitutive model that incorporates both instantaneous and delayed irreversible components of the rock material. For this purpose, the present analysis considers a constitutive model that includes both instantaneous plasticity to describe short-term material yielding and viscoplasticity to represent delayed behavior. The formulation of the coupled plasticity-viscoplasticity rheological model is based on that originally proposed in [21] and [29]. Previous studies have implemented this plastic-viscoplastic model for computational analysis of deformation in single tunnels (e.g., [6, 23, 16, 25]). For the sake of brevity, only

the main features of this constitutive model shall be summarized below. Detailed description of the model, including application and validation in the context of single tunnel structures may be found in [27]. Finite element implementation of this model in the USERMAT procedure of ANSYS software is also described in [25].

The elastoplastic-viscoplastic model is formulated based on a serial association of the elastoplastic and viscoplastic constitutive models. The local strain rate $\dot{\epsilon}$ is split into three contributions $\dot{\epsilon} = \dot{\epsilon}^e + \dot{\epsilon}^p + \dot{\epsilon}^{vp}$, so that the constitutive relationships relating the Cauchy stress rate $\dot{\sigma}$ and strain rate components can be written as:

$$\dot{\sigma} = \mathbf{D} : \dot{\epsilon}^e = \mathbf{D} : (\dot{\epsilon} - \dot{\epsilon}^p - \dot{\epsilon}^{vp}). \quad (1)$$

In the above relationship, $\dot{\epsilon}^e$, $\dot{\epsilon}^p$ and $\dot{\epsilon}^{vp}$, represent respectively the elastic, plastic and viscoplastic strain rate, and \mathbf{D} denote the fourth-order isotropic elastic linear constitutive tensor. The one-dimensional representation in Fig. 1 shows this association. In this model is used a Drucker-Prager plastic flow surface given by

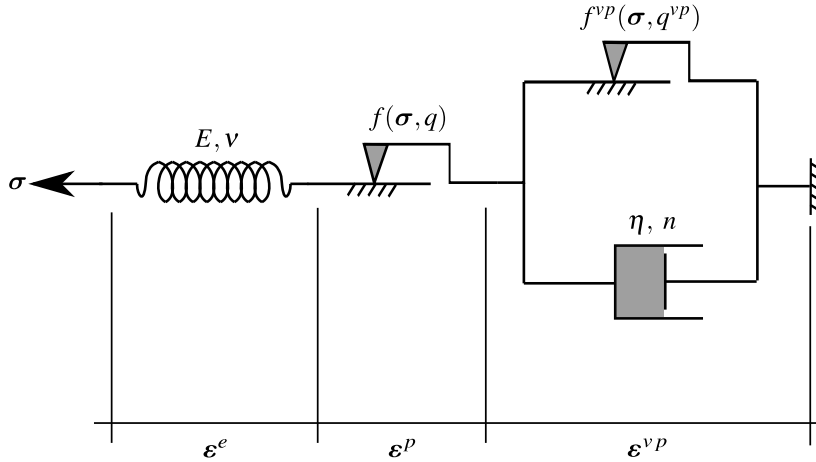


Figure 1: Rheological representation of the elastoplastic-viscoplastic model.

$$f(\sigma, q) = f(I_1, J_2, q) = \beta_1 I_1 + \beta_2 \sqrt{J_2} - q(\alpha), \quad (2)$$

which I_1 is the first invariant of the stress tensor, J_2 the second invariant of the deviator tensor and β_1 , β_2 and $q(\alpha)$ are strength parameters related to the friction angle ϕ and cohesion $c(\alpha)$, respectively. In the present model Drucker-Prager surface been inner of the Mohr-Coulomb surface [5], that is,

$$\beta_1 = \frac{(k-1)}{3}, \quad \beta_2 = \frac{(2k+1)}{\sqrt{3}}, \quad q(\alpha) = 2\sqrt{k} c(\alpha), \quad (3)$$

where $k = (1 + \sin \phi)/(1 - \sin \phi)$. The internal variable α is the equivalent plastic strain $\bar{\epsilon}^p$ used to simulate strain hardening/softening phenomena. However, for this study, we adopt perfect plasticity, meaning that c is a constant. For the viscoplasticity surface f^{vp} the same surface is employed, but with ϕ^{vp} in β_1 and β_2 , and $q^{vp} = 2\sqrt{k^{vp}} c^{vp}$ where $k^{vp} = (1 + \sin \phi^{vp})/(1 - \sin \phi^{vp})$ and c^{vp} is a constant, i.e., perfect viscoplasticity. The plastic flow rule is given by:

$$\dot{\epsilon}^p = \begin{cases} \dot{\lambda} \frac{\partial g}{\partial \sigma} & \text{for } f > 0 \\ \mathbf{0}, & \text{for } f \leq 0 \end{cases}, \quad (4)$$

where $\dot{\lambda}$ is the plasticity multiplier and g is a potential flow function analogous to f used to simulate the volume dilatation during the evolution of plastic deformations. However, for this analysis, was used associated plasticity, i.e., $g = f$. The plastic multiplier is obtained through the consistency condition $\dot{f} = 0$. Numerical details of this implementation can be found in [27]. For viscoplastic flow rule we have,

$$\dot{\epsilon}^{vp} = \dot{\lambda}^{vp} \frac{\partial f^{vp}}{\partial \sigma} \quad (5)$$

In contrast to the plastic multiplier, the viscoplastic multiplier λ^{vp} is independent of a consistency like condition. As a result, its expression is explicit. Based on the framework of generalized Perzyna's overstress theory [22], its expression may be derived as follows:

$$\dot{\lambda}^{vp} = \frac{\Phi(\sigma, q^{vp})}{\eta} \quad \text{and} \quad \Phi = \left\langle \frac{f^{vp}(\sigma, q^{vp})}{f_0} \right\rangle^n, \quad (6)$$

where Φ is the overstress function, η is the dynamic viscosity constant, n is the dimensionless parameter that gives the form of the power law, f_0 a parameter conveniently adopted and $\langle * \rangle$ is the McCauley function which is 0 when $* < 0$, i.e. viscoplastic flow will only occur when the overstress function is positive.

In this coupled model, when $\phi = \phi^{vp}$, cohesion entirely controls the evolution of local mechanical fields. Specifically, when $c \rightarrow \infty$ and $c^{vp} \rightarrow \infty$, the system achieves a purely elastic solution. The solution becomes purely elastoviscoplastic with $c \rightarrow \infty$, while a pure elastoplastic solution emerges with $c^{vp} \rightarrow \infty$. In the coupled analysis, condition $c^{vp} < c$ is adopted, allowing the viscoplastic domain to occur without plasticity. However, in the presence of plasticity, viscous effects become inevitable. Fig. 2 illustrates these domains in principal stress space.

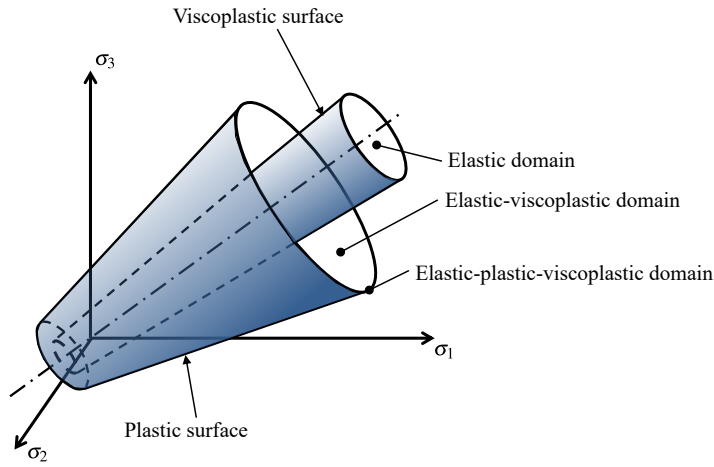


Figure 2: Elastoplastic-viscoplastic domains.

4. Constitutive Model of the Lining

Shrinkage and creep phenomena represent fundamental components of concrete deformation processes that are expected to naturally affect the instantaneous as well as the transient and long-term behavior of structures involving such material. However, most of the tunnel design analyses consider the concrete involved in lining systems as a linear elastic material. From a phenomenological point of view, creep of concrete refers to the time-dependent deformation induced by sustained loading, whereas shrinkage deformation refers to the volume decrease caused by drying. As far as deformation in tunnel structures is concerned, creep and shrinkage have an important effect on the performance of the concrete lining and consequently on its contribution to controlling the long-term convergence of the tunnel. To account for such constitutive features, the concrete creep deformation is addressed by means of an aging viscoelastic rheological model relying on Bažant and Prasannan Solidification Theory [3, 4]. The viscoelastic model is described by a Generalized Kelvin-chain [28, 26] (show in Fig. 3) whose defining parameters are calibrated based on the CEB-FIP MC90 standard specifications formulation reported in [8]. As regards the concrete deformation associated with shrinkage, the isotropic formulation proposed in CEB-FIP MC90 standard [8] is adopted in the present modelling and subsequent computational analyses. Full details regarding model definition and related finite element implementation may be found in [24] and [26].

Accordingly, the constitutive equations for concrete lining relating the stress and strain rate can be expressed in the framework of infinitesimal strain analysis as:

$$\dot{\sigma} = \mathbf{D} : \dot{\epsilon}^e = \mathbf{D} : \dot{\epsilon} - \mathbf{D} : \dot{\epsilon}^{sh} - \mathbf{D}^* : \dot{\epsilon}^{cr} \quad (7)$$

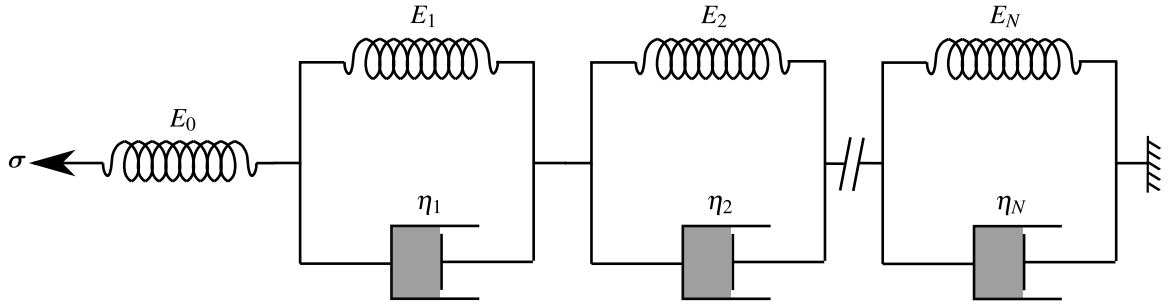


Figure 3: Rheological representation of the viscoelastic model.

In the above relationship, $\dot{\epsilon}^{sh}$ and $\dot{\epsilon}^{cr}$ are respectively the shrinkage and creep strain rates. The fourth-order tensors \mathbf{D} and \mathbf{D}^* refer to the isotropic elastic linear constitutive tensor and modified constitutive tensor that incorporate the aging viscoelastic properties of the concrete, respectively.

For the numerical implementation purposes, relationship (7) may conveniently be written in incremental form:

$$\Delta \boldsymbol{\sigma} = \mathbf{D} : \Delta \boldsymbol{\epsilon} - \mathbf{D} : \Delta \boldsymbol{\epsilon}^{sh} - \mathbf{D}^* : \Delta \boldsymbol{\epsilon}^{cr} \quad (8)$$

As mentioned above, isotropic formulation is considered for shrinkage, so that increment of shrinkage strain reads:

$$\Delta \boldsymbol{\epsilon}^{sh} = \Delta \epsilon_{sh}(t_s) \mathbf{1} \quad (9)$$

where t_s represents the concrete curing time, and $\Delta \epsilon_{sh}$ is the variation in magnitude of the concrete deformation associated with shrinkage (the dependency $\Delta \epsilon_{sh}$ of on current time is omitted). The latter expression is determined based on CEB-FIP MC90 standard specifications [8]. The increment of creep strain $\Delta \epsilon^{cr}$ is computed making use of the incremental algorithm developed by Bažant and Prasannan [3; 4], together with a model calibration that incorporates CEB-FIP MC90 standard formulation [8]. The latter procedure for model parameters identification is achieved by comparing the creep functions provided in references [3; 4] and [8], leading to the following equivalence:

$$E_0 = E_c(t_0), \quad \gamma(t - t_0) = \beta_c(t - t_0), \quad \frac{1}{v(t)} = \frac{\phi_0}{E_{ci}} \quad \text{and} \quad \frac{1}{\eta(t)} \rightarrow 0 \quad (10)$$

in which t refers to the current time value and t_0 to the concrete age at the instant of load application (time interval $t - t_0$ is generally referred to as loading time or loading age). In Bažant and Prasannan [3; 4] model, E_0 is the instantaneous elasticity modulus of the concrete formed aggregates and cement paste particles, $\gamma(t - t_0)$ is the microviscoelastic deformation of the volume fraction $v(t)$ of solidified concrete and $\eta(t)$ is the apparent macroscopic viscosity. In the CEB-FIP MC90 formulation [8], $E_c(t_0)$ stands for the tangent elastic modulus of concrete at the instant of the loading application t_0 , $\beta_c(t - t_0)$ is a coefficient that depends on the loading age $t - t_0$, $\phi_0(t_0)$ is a coefficient depending on the age t_0 of the concrete and E_{ci} represents the tangent elasticity modulus of the concrete at the age of 28 day.

5. Spatial and time discretization of the domain

The geometric layout of the modeled domain Ω consists of a twin deep tunnel with a transverse gallery, as shown in Fig. 4.

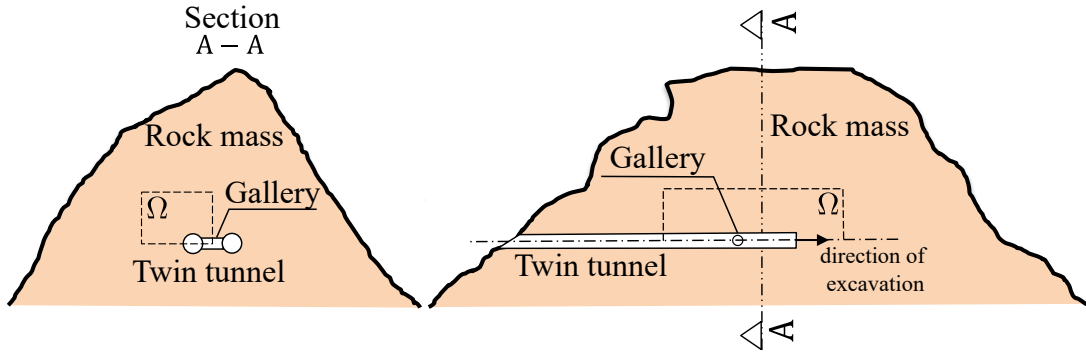


Figure 4: Geometric layout of the domain

This domain is parameterized based on the radius of the longitudinal tunnel R_i . The geometric parameters and boundary conditions for the domain problem are shown in Fig. 5. We considered front, side, and bottom symmetry to reduce computational cost. In this domain, d_1 is the distance between longitudinal tunnels axes, L_2 total excavated length, d_3 domain height, L_1 length of the unexcavated region, L_3 transversal length of the domain, L_p step length of the excavation process, d_2 position of the gallery along the longitudinal tunnel. Together with boundary pressure σ_x, σ_y and σ_z , we apply the initial stress condition $\sigma_0 = -\sigma_x e_x \otimes e_x - \sigma_y e_y \otimes e_y - \sigma_z e_z \otimes e_z$ at all integration points to simulate the initial state of the rock mass. The spatial discretization in Fig. 5 corresponds to a mesh with trilinear hexahedral elements (SOLID 185, 8 nodes), except in the gallery region, which uses higher-order tetrahedral elements (SOLID186, 10 nodes). We divided the mesh into two regions: one near the tunnel (light gray), which we refined more,

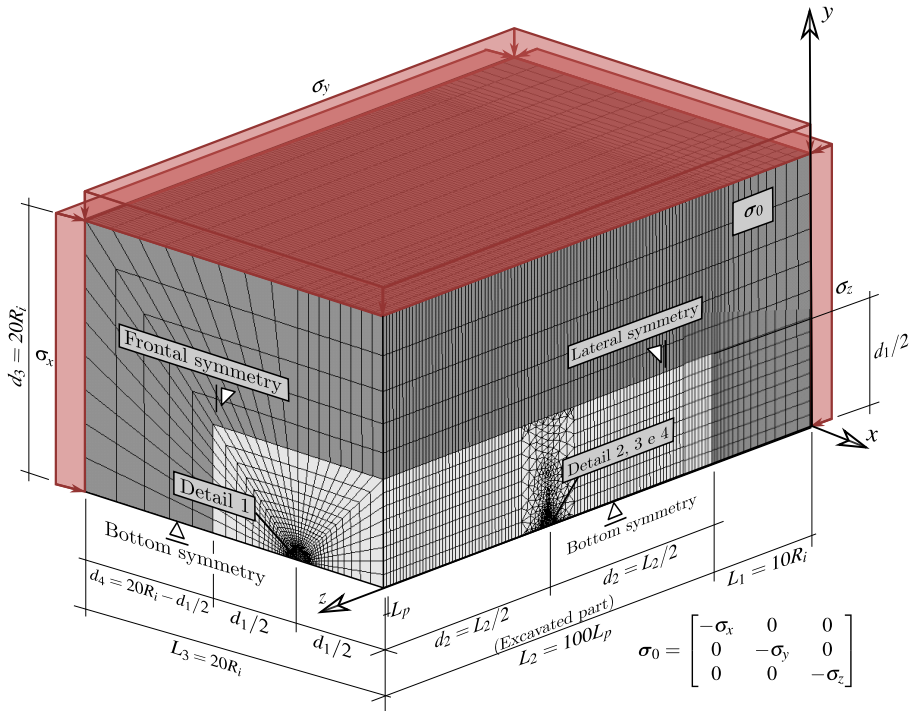


Figure 5: Mesh, dimensions and boundary conditions of the 3D twin tunnel domain

and a region farther away (dark gray), which we increased the aspect ratio to minimize the number of elements in that region. Due to the low deformation gradient away from the tunnel wall, elements in this area can be considerably larger

than in other regions. Fig. 6 presents the mesh at the cross-section of the longitudinal tunnel, with e representing the thickness of the lining.

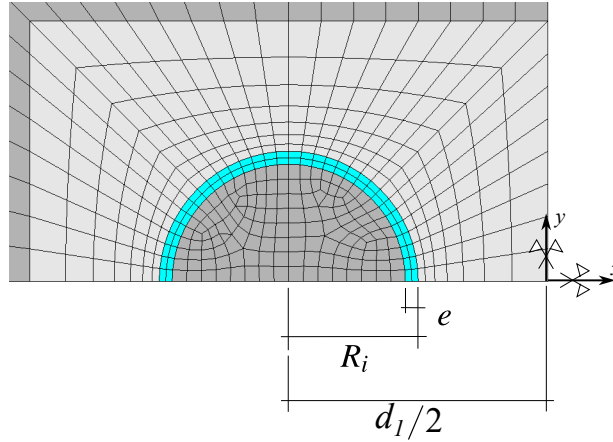


Figure 6: Detail 1 - Mesh in longitudinal tunnel cross-section with spacing $d_1 = 4R_i$

One of the aspects investigated in this work is the influence of the spacing d_1 in the convergence of the longitudinal twin tunnel. Fig. 7 and Fig. 8 illustrate the spatial discretization in the gallery region and its connection with the longitudinal tunnel considering spacings $d_1 = 16R_i$, $8R_i$ and $4R_i$, respectively. We adopt the radius of the gallery as $2/3R_i$, and its lining has the same material and thickness as the longitudinal tunnel. The dimensions d_5 and d_1 define the size of the transition region comprising tetrahedral elements between the gallery and the rest of the domain. Fig. 9 shows half of this transition region inside the rock mass.

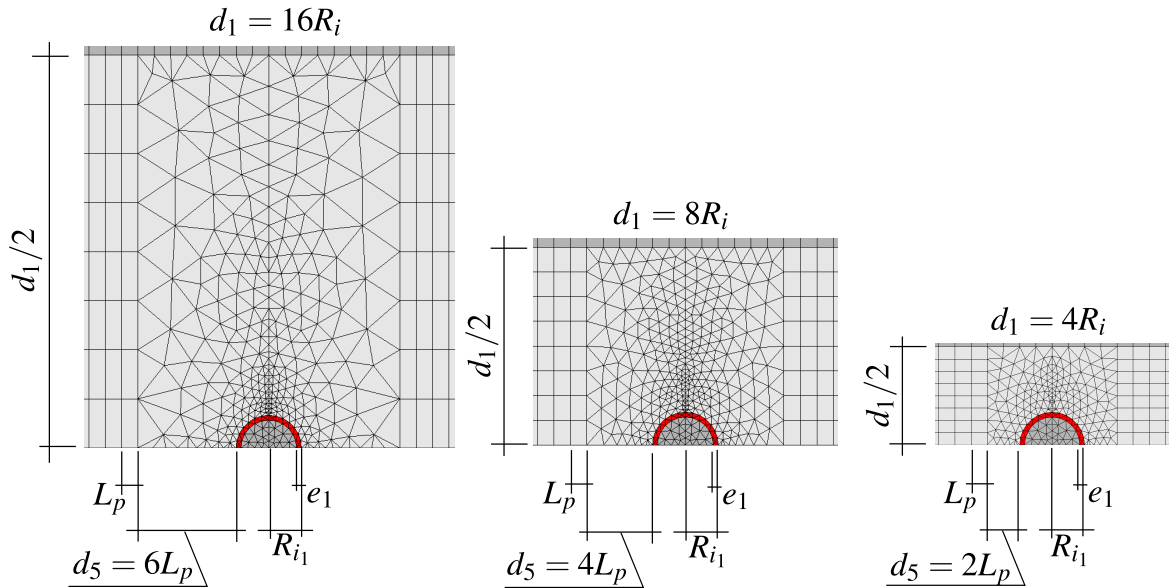


Figure 7: Detail 2 - Side view of the mesh in gallery region with $d_1 = 16R_i$, $d_1 = 8R_i$ and $d_1 = 4R_i$

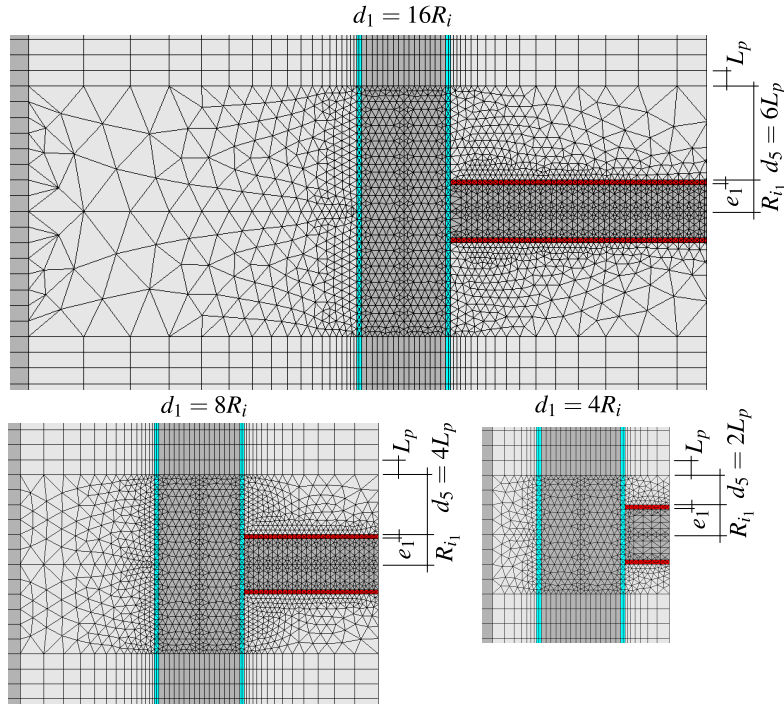


Figure 8: Detail 3 - Bottom view of the mesh in gallery region with $d_1 = 16R_i$, $d_1 = 8R_i$ and $d_1 = 4R_i$

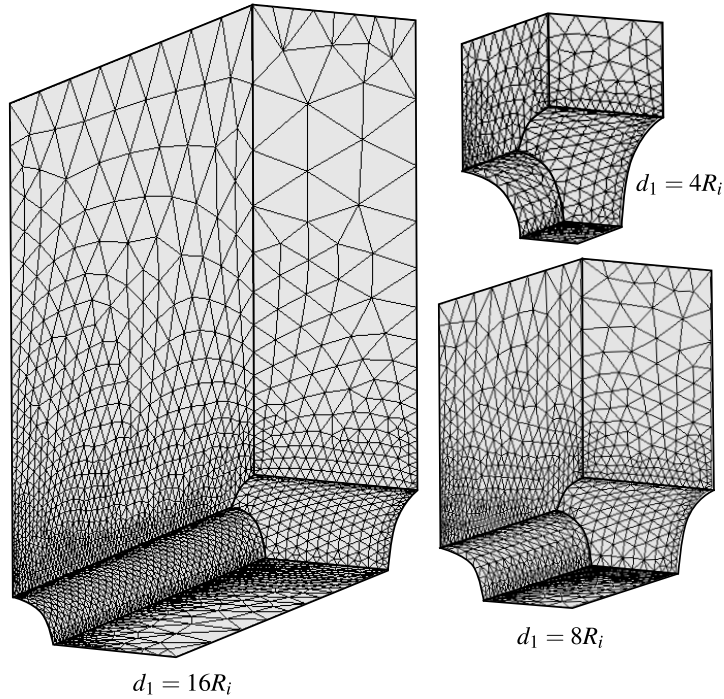


Figure 9: Detail 4 - Isometric view of the portion of the mesh in gallery transition region $d_1 = 16R_i$, $d_1 = 8R_i$ and $d_1 = 4R_i$

Fig. 10 shows the mesh of the lining at the junction of the gallery and the longitudinal tunnel for $d_1 = 4R_i$, $8R_i$, and $16R_i$. One noteworthy characteristic of this mesh is that it confines the tetrahedral elements within the contour of every excavation step.

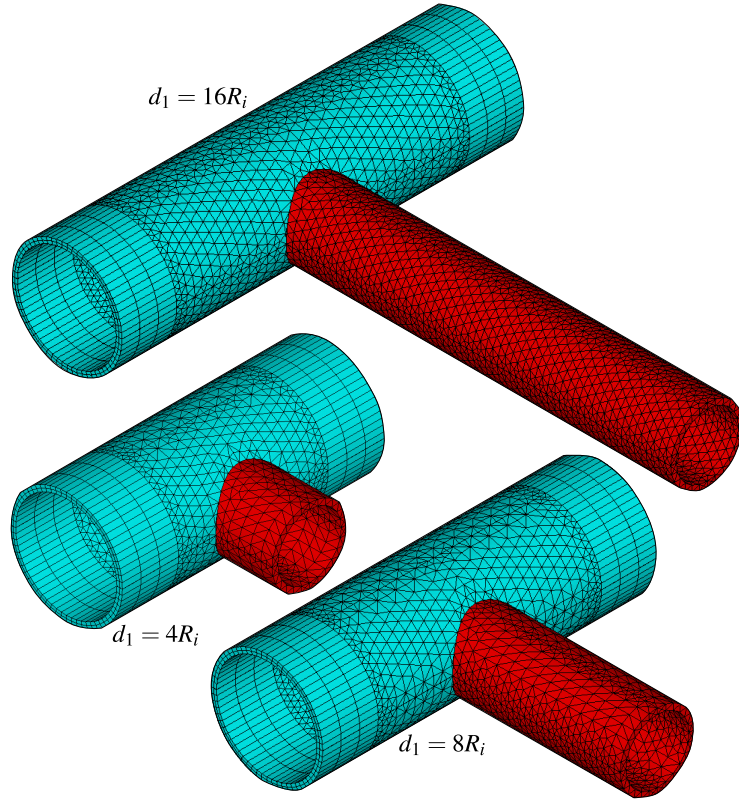


Figure 10: Isometric view of the lining at the intersection for $d_1 = 16R_i$, $d_1 = 8R_i$ and $d_1 = 4R_i$ - expansion of symmetry in the xz plane

The construction process is simulated through the deactivating and activating method, i.e., in each step of excavation, reducing the stiffness of the excavated element (multiply by $1E-8$) and active the lining elements at a distance d_0 from the excavation face (unlined length). With each excavation step, we execute the solution, and time advances based on the expression $t_p = L_p/V_p$, where L_p represents the length of the excavation step, and V_p is the speed of the excavation face. Fig. 11 illustrates a schematic of the excavation process where n_p is the number of excavation steps. In this Figure, n_{pig} represents the number of steps excavated in the longitudinal tunnel that starts gallery excavation. Once reaching this step, we pause the excavation of the longitudinal tunnel, and the gallery excavation begins. In the gallery, L_{p1} is the step length of the gallery excavation, V_{p1} is the speed of the gallery excavation, and d_{01} is the unlined length of the gallery. After completing the gallery excavation, the longitudinal tunnel excavation resumes. These parameters related to the geometry domain, excavation and installation of the lining are shown in Table 1.

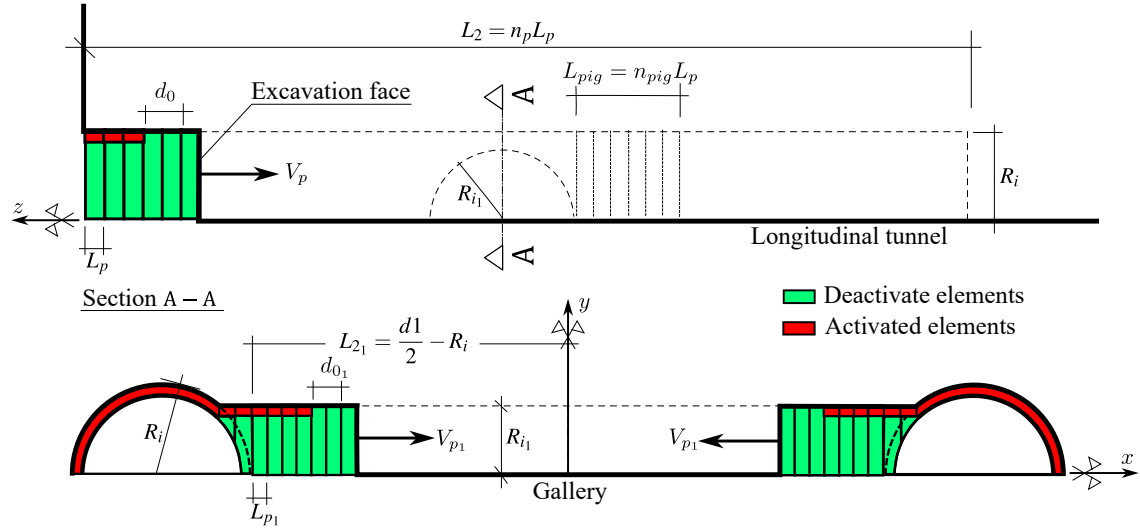


Figure 11: Schematic of the excavation process

Table 1

Parameters related to the geometry of the domain, excavation and installation of the lining

| PARAMETERS | SYMBOL | UNIT | VALUES |
|--|-----------|-------|--|
| Longitudinal tunnels | | | |
| Radius of the longitudinal tunnel | R_i | m | R_i |
| Thickness of the lining | e | m | $0.1 R_i$ |
| Step length of the excavation process | L_p | m | $1/3 R_i$ |
| Unlined length | d_0 | m | $2 L_p$ |
| Speed of the excavation face | V_p | m/day | 12.5 |
| Excavation step time | t_p | day | L_p / V_p |
| Gallery | | | |
| Radius of the gallery | R_{i1} | m | $2/3 R_i$ |
| Thickness of the concrete lining | e_1 | m | $0.1 R_i$ |
| Step length of the excavation process ¹ | L_{p1} | m | $0.3 R_{i1}$ $0.3214 R_{i1}$ $0.3387 R_{i1}$ |
| Unlined length | d_{01} | m | $2 L_{p1}$ |
| Speed of the excavation face | V_{p1} | m/day | 12.5 |
| Number of steps that starts gallery excavation | n_{pig} | un | 15 |
| Rest of domain | | | |
| Distance between longitudinal tunnel axes | d_1 | m | $4 R_i$ $8 R_i$ $16 R_i$ |
| Length of the unexcavated region | L_1 | m | $10 R_i$ |
| Total excavated length | L_2 | m | $100 L_p$ |
| Domain height | L_3 | m | $20 R_i$ |

¹ $L_{p1} \approx 1/3 R_{i1}$ in such a way that there are n integer excavation steps in $d_1 - 2 R_i$

During tunnel construction, we determine the initial time increment for solution steps as $0.5t_p$ (for the longitudinal tunnel) and $0.5t_{p1}$ (for the transverse gallery). ANSYS manages the time increment using the bisection method, halving the time step if there is no equilibrium convergence.

After tunnel excavation, in time-dependent constitutive models, time continues to progress to capture long-term viscous effects. In this stage, each time step lasts 100 days, with an initial increment of 50 days. This increase, compared to the excavation time increments, is facilitated by the semi-implicit scheme in the viscoplasticity solution. The explicit scheme, as indicated in [31], requires a smaller time increment to the precision of the solution.

6. Comparison with analytical solutions

To examine mesh convergence and validate the numerical model, we compared the numerical solution with the elastic and elastoplastic analytical solution in the plane state of deformations for twin tunnels. Guo et al. [17] develop an elastic analytical solution for the stress field around twin circular tunnels with hydrostatic pressure using the complex variable and the superposition principle. The Fig. 12 shows the tangential stress distribution around the tunnel's boundary in this analytical solution with the numerical solution considering $R_i = 4$ m, $E = 500$ MPa, $\nu = 0.23$, $d_1 = 2R_i$, $\sigma_x = \sigma_y = \sigma_z = 2.2$ MPa.

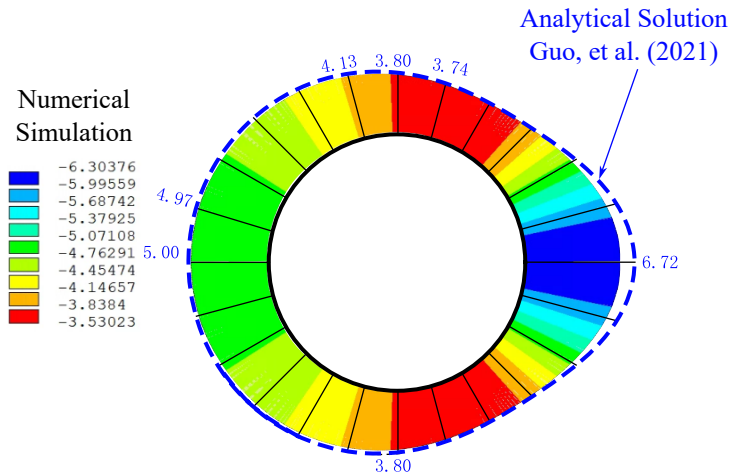


Figure 12: Verification of numerical results of orthoradial stresses with the analytical solution

Ma et. al. [18] developed an analytical solution for a perfectly plastic constitutive model with a Mohr-Coulomb surface. One of the results was the contour of the plastic zone for several conditions. Fig. 13 shows the comparison between the numerical model solution (taken from a section away from the excavation face) and the analytical solution. For these analysis, $R_i = 1$ m, Young's modulus $E = 20$ GPa and Poisson's ratio $\nu = 0.3$.